Research Square

Preprints are preliminary reports that have not undergone peer review.
They should not be considered conclusive, used to inform clinical practice,
or referenced by the media as validated information.

# Correlating structural and chemical transitions in the oxidation of Th-doped UO2

**Florence Legg**

florence.legg@esrf.fr

XMaS Beamline

**Eleanor Lawrence Bright**

The Rossendorf Beamline

**Lottie Harding**

University of Bristol

**Didier Wermeille**

XMaS Beamline

**Jude Laverock**

University of Bristol

**Erin Hollington**

University of Bristol

**Hayley Green**

Sellafield Ltd.

**Helen Steele**

Sellafield Ltd.

**Ross Springell**

University of Bristol

**Article**

**Keywords:**

**Posted Date:** November 13th, 2026

**DOI:** https://doi.org/10.21203/rs.3.rs-11303786/v1

**License:** This work is licensed under a Creative Commons Attribution 4.0 International License.
Read Full License

**Additional Declarations:** No competing interests reported.

# Correlating structural and chemical transitions in the oxidation of Th-doped $UO_2$

Florence Legg[a,b,c,*], Eleanor Lawrence Bright[d,e], Lottie M. Harding[a], Didier Wermeille[b,c], Jude Laverock[f], Erin Hollington[a], Hayley Green[g], Helen Steele[g], Ross Springell[a]

[a]*School of Physics, University of Bristol, Tyndall Avenue, Bristol BS8 1TL, UK*
[b]*XMaS Beamline, European Synchrotron Radiation Facility, Grenoble, France*
[c]*Department of Physics, University of Liverpool, The Oliver Lodge, Liverpool L69 7ZE, UK*
[d]*The Rossendorf Beamline, European Synchrotron Radiation Facility, Grenoble, France*
[e]*Institute of Resource Ecology, Helmholtz-Zentrum Dresden Rossendorf, 01328 Dresden, Germany*
[f]*School of Chemistry, University of Bristol, Cantock's Close, Bristol BS8 1TS, UK*
[g]*Sellafield Limited, Cumbria, CA20 1PG, UK*

*Keywords:* Actinide oxides, mixed oxides, oxidation, XPS, XRD, XAS, $UO_2$, spent-fuel

**Abstract**

The oxidative phase transition of $UO_2$ occurs via formation of several intermediate phases, leading to significant structural and chemical changes in the material. This can increase fuel solubility, complicating the long-term storage of spent nuclear fuel. The incorporation of thorium into $UO_2$ and the effect on oxidation is of particular interest, as thorium exists primarily as Th(IV) making it resistant to the formation of higher oxide phases. Here, we investigate the influence of Th content on oxidation behaviour in epitaxial thin films. Complementary *in situ* synchrotron experiments were conducted to probe the crystallographic and chemical-state changes throughout oxidation, allowing correlation of the changing oxide structure to the evolving uranium valency. Overall results demonstrate that oxidation is fully inhibited with 13% Th. These results provide new insight into the coupled structural and chemical transformations in homogeneous U-Th solid solutions, supporting the use of mixed actinide oxides as a spent-fuel storage solution.

## 1. Introduction

Uranium dioxide ($UO_2$) is the most prevalent nuclear fuel in the commercial nuclear energy sector. Significant research has historically been applied to understand its various chemical and structural properties under both conditions relevant to its use as a nuclear fuel and in longer-term storage environments. The oxidative phase transition of $UO_2$ to $U_3O_8$ is associated with an increase in solubility and significant volume expansion, complicating the safe and secure storage of spent nuclear fuel [1, 2]. This transition goes through five distinct phases, with initial formation of $UO_{2+y}$ at room temperature. The intermediate oxide phases $U_4O_9$ and $U_3O_7$ form at $y$ = 0.25 and $y$ = 0.33, respectively [3]. The formation of the $U_4O_9$ intermediate oxide phase occurs as an accumulation of oxygen in interstitial sites within the fluorite structure, along with a distortion of the cubic lattice, leading to the formation of an ordered superstructure with cubic symmetry, having an approximate composition of $U_{64}O_{143}$ [4]. As oxidation progresses, the formation of additional oxygen clusters cause further distortions in the lattice forming $U_3O_7$, a distorted fluorite structure with a tetragonal symmetry. The $U_3O_8$ phase forms as an orthorhombic structure where $y$ = 0.67.

*Corresponding author
*Email address:* florence.legg@esrf.fr (Florence Legg)

This structural transformation is also associated with changes to the U valency, where uranium will exist as U(IV) in stoichiometric $UO_2$. Increased incorporation of oxygen in interstitial sites in the intermediate oxides is balanced by an increase in U(V), with a mixed U(IV):(V) valency present in both $U_4O_9$ and $U_3O_7$. Transformation to $U_3O_8$ is combined with the formation of U(VI), with an approximate 2:1 U(V):(VI) ratio [5]. This transformation stage increases the solubility of the oxide, due to U(VI) being soluble in water, increasing the risk of a breach in containment in a long-term waste storage environment.

Mixed actinide oxides (MOx) can be employed as alternative nuclear fuels and for waste storage applications [6, 7]. The incorporation of thorium into the $UO_2$ lattice and the resultant effect on the oxidative phase transition is of particular interest, as thorium exists primarily in the Th(IV) oxidation state, making it resistant to the formation of higher oxide phases [8]. This potential to provide enhanced resistance to oxidation has implications for the improved stability of spent nuclear fuel. Existing studies suggest that thorium incorporation can significantly impact the oxidation of $UO_2$ [6, 9, 10]. Furthermore, Rickert *et al.* [11] observed as little as 10% thorium was sufficient to prevent oxidation to the $U_3O_8$ phase in bulk (U,Th)$O_2$ single crystals, however oxidation to intermediate phases is still observed in ($U_xTh_{1-x}$)$O_2$ samples where $x$ = 0.75 and 0.90.

In this work, we utilise epitaxial thin films of [0 0 1]-oriented ($U_xTh_{1-x}$)$O_2$ providing a high degree of homogeneity [12], allowing us to systematically study the degree of oxidation with respect to thorium composition. Epitaxial thin films can be used to accurately model the ideal surface of a material allowing access to crystals comprised of a single orientation, in this case allowing us to exploit the topotactic phase transition of $UO_2$ to $U_3O_8$ [13] . This also gives us insight into parts of the oxidation mechanism under highly controlled conditions which would be inaccessible using other sample types. Additionally, a number of film properties such as dopant concentration, film stoichiometry and lattice strain can be intentionally implemented during fabrication, allowing investigation of unique properties which would be inaccessible using other methods [3, 12, 14–16].

For this study, we utilise a combination of synchrotron techniques conducted *in situ* to study both the structural and chemical transformations occurring in the system. By applying these techniques, we have access to sensitive and high resolution measurements of the oxide transition, providing keen insight into the influence of Th composition on the transformation, and allowing a more detailed analysis of any intermediate oxide phases that may form. The results from this study therefore aim to inform the future use of U-Th MOx in the nuclear fuel cycle, with a focus on understanding its long-term stability as a waste form.

## 2. Results

### *2.1. In-situ structural characterisation*

Epitaxial thin films of [0 0 1]-oriented ($U_xTh_{1-x}$)$O_2$ were investigated via *in situ* oxidation. Measurements were conducted on the ID11 and BM28 (XMaS) beam lines at the European Synchrotron Radiation Facility (ESRF). The structural transformations were measured as 2D mappings of still XRD images, converted to reciprocal space maps (RSM) for analysis.

RSM taken out-of-plane with respect to the film surface ($Q_x = Q_y$ direction, along the (hhl) plane), showing oxidation of the ($U_{0.98}Th_{0.02}$)$O_2$ sample at several temperature stages are shown in Figure 1. The RSM taken at

room temperature indicates that the sample is epitaxial and of a high crystalline quality. $CaF_2$ and $UO_2$ share an FCC $Fm\bar{3}m$ structure and lattice parameters of 5.463 Å [17] and 5.471 Å [18], respectively. Therefore, the Bragg reflections overlap significantly making it difficult to isolate the individual peaks, hence the consistent high intensity peaks shown throughout heating. Formation of the intermediate crystalline phase of $U_4O_9$ can be observed in the RSM at 230°C, indicated by the weak, sharp reflections with a quadrupling of the lattice parameter. Further heating to 360°C shows initial formation of $U_3O_8$, indicated by significantly broader reflections. Further heating to 390°C sees an increase in the size and intensity of $U_3O_8$ reflections, where only $CaF_2$ substrate reflections remain as well as the higher oxide. Notably, there are no clear reflections which can be attributed to $U_3O_7$ in the $Q_x = Q_y$ maps.

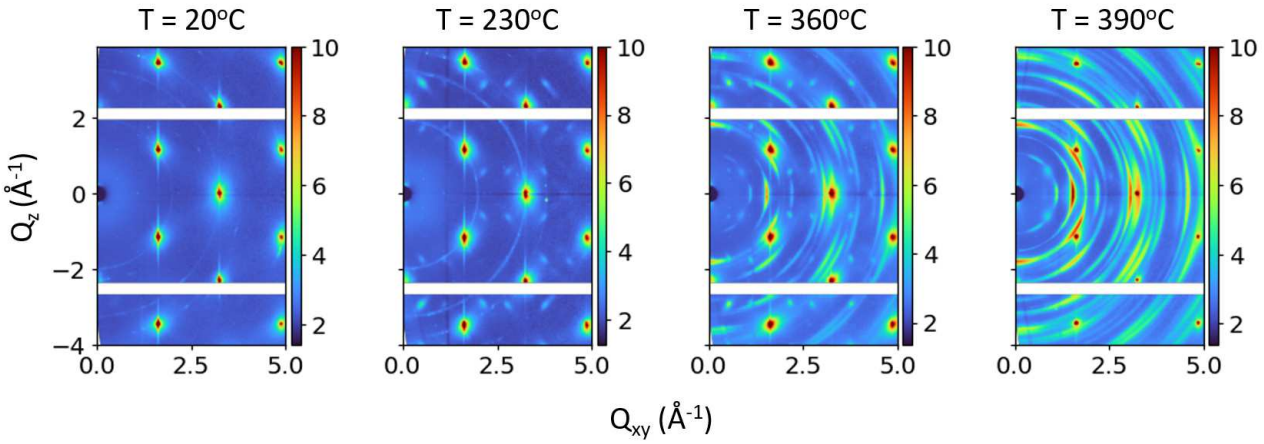



Figure 1: RSM showing the oxidation of [0 0 1]-oriented $(U_{0.98}Th_{0.02})O_2$ sample at 20°C, 230°C, 360°C and 390°C. Slices have been taken from the $Q_x = Q_y$ plane, showing the $(hhl)$ slice of the actinide oxide structure.

The observed peak broadening for the $U_3O_8$ phase is due to a mismatch in the topotactic transformation from the (001) of $UO_2$ to the (130) of $U_3O_8$ predominantly observed in the out-of-plane axis [19]. This mismatch will likely introduce significant stress in this direction, reducing the crystalline quality of the $U_3O_8$ formed. This broadening of the $U_3O_8$ reflections around the $Q$-direction is also observed more significantly for out-of-plane RSM compared to in-plane, where the reflections are much sharper. The $U_3O_8$ reflections formed for the $(U_{0.98}Th_{0.02})O_2$ sample show no observable differences to that observed for $UO_2$ in [19].

Figure 2 shows an experimental $Q_x = Q_y$ map for the $(U_{0.98}Th_{0.02})O_2$ sample at 298°C, compared to a calculated (hhl) map for the $\beta$-$U_4O_9$ phase, with the structure taken from [20]. The $U_4O_9$ phase is an ordered superstructure due to the long-range ordering of oxygen interstitial sites, formed through the creation of cuboctahedral oxygen clusters [4, 21] causing distortions of the fluorite-like structure and a deviation from cubic symmetry. Diffraction patterns of crystals with such superstructures often display parent structure reflections with a higher intensity along with weaker satellite reflections corresponding to a deviation from the parent structure, as shown in Figure 2. Overall, the weaker superstructure reflections observed in the experimental map are consistent with the $\beta$-$U_4O_9$ reflections in the calculated map. However, there are several observable differences compared to the expected reflections. The experimental $U_4O_9$ reflections exhibit significant broadening along the [1 1 1] axis, suggesting shorter-range ordering in this plane. This broadening is also characterised by a sharper higher intensity part of the peak and a weaker, broader part of the peak, suggesting domains of different ordering length-scales.

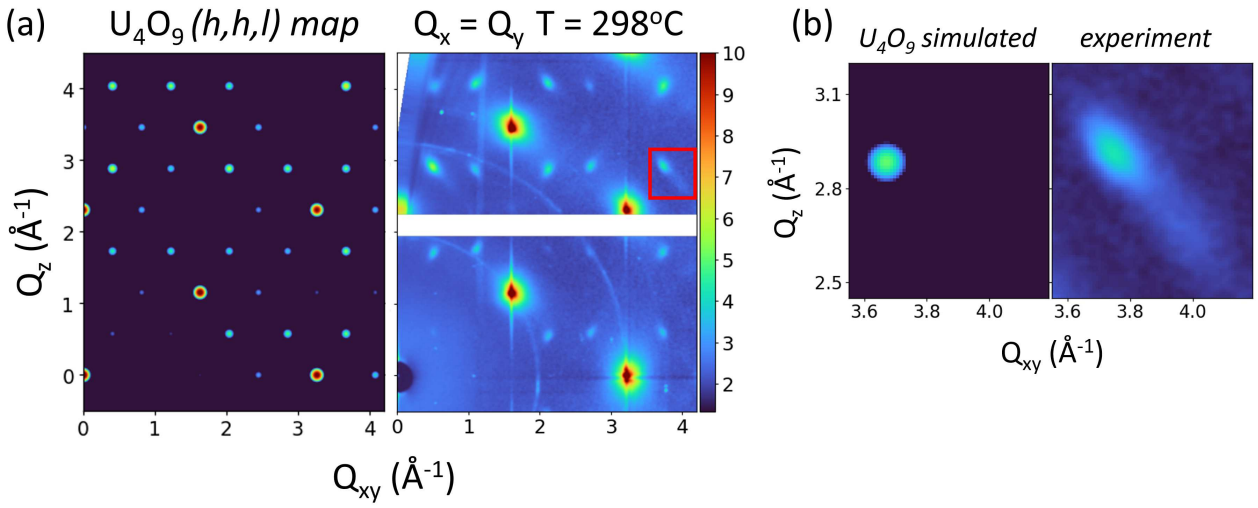



Figure 2: (a) Simulated RSM of $U_4O_9$ structure [20] compared to experimental map for the $(U_{0.98}Th_{0.02})O_2$ sample at 298°C. (b) A close up of one $U_4O_9$ reflection is shown in the experimental map (as indicated by the red square), compared to the equivalent simulated reflection.

Figure 3 (a) shows an experimental $Q_y = 0$ map for the $(U_{0.98}Th_{0.02})O_2$ sample at 313°C, compared to a calculated map for $U_3O_7$ derived from [4], showing all expected domains. As oxidation progresses an increased density of interstitial oxygen clusters causes further distortions and deviations from the FCC structure. The tetragonal $U_3O_7$ structure forms from a breaking of the cubic symmetry present for the $UO_2$ and $U_4O_9$ phases, indicated in the calculated map by a splitting of the strong FCC reflections [19]. There are several low intensity reflections in the experimental map which are assumed to be due the $U_3O_7$ structure. As shown in the close-up sections in 3 (b), the position of the reflections shown in the experimental map and the $U_3O_7$ simulated map do not match perfectly, in addition to there being several mismatched reflections in both the simulated and experimental map. Furthermore, The expected highest intensity reflections, appearing as splitting of the parent FCC structure reflections, do not appear to be present. An additional comparison to the equivalent area in the $U_4O_9$ simulated map is given, suggesting these reflections are not due to the $U_4O_9$ superstructure. No further $U_3O_7$ reflections were observed for the in-plane RSM, at any other temperature or for any other sample measured in this study.

Figure 4 shows the out-of-plane $Q_x = Q_y$ RSM for the $(U_{0.87}Th_{0.13})O_2$ sample taken at 20°C, 230°C, 360°C and 390°C. There are some small changes in the overall background intensity and intensity of the Bragg peaks throughout heating, likely due to environmental changes and differences in alignment. However, there are no structural changes or formation of higher oxide phases. This suggests that no oxidation has taken place, and indicates that the Th threshold for preventing the expected oxidative phase transition has been reached.

### 2.2. *Chemical characterisation results*

X-ray adsorption near edge structure (XANES) measurements were conducted *in situ* at the U $L_3$-edge as a function of temperature. Fitted XANES spectra taken *in situ* at the U $L_3$-edge on the XMaS beamline for an [0 0 1]-oriented

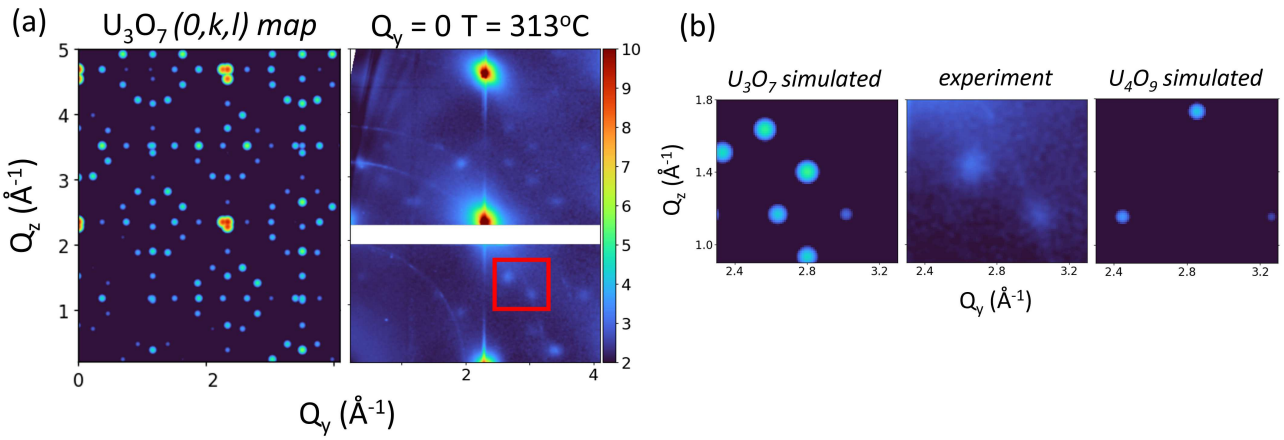



Figure 3: (a) Simulated RSM of the $U_3O_7$ structures [4] compared to an experimental map for the $(U_{0.98}Th_{0.02})O_2$ sample at 313°C. (b) A close up of two reflections as indicated in the experimental map by the red square, compared to the equivalent area for simulated $U_3O_7$ and $U_4O_9$ maps.

$UO_2$ sample are shown in Figure 5 (a) for the initial and final temperature stages. White line positions ($E_{WL}$) were determined by taking the first derivative of the fit and determining the maxima. There is a significant shift in $E_{WL}$ and peak broadening associated with increasing temperature, where $E_{WL,25^oC}$ = 17.157 keV and $E_{WL,340^oC}$ = 17.160 keV corresponding to a shift of 3 eV. This shift can be attributed to the formation of U(VI) and the mixed uranium valency, which also correlates to the structural transformation to $U_3O_8$. This shift in $E_{WL}$ and peak broadening is indicative of $U_3O_8$ formation and is observed in other studies [22, 23]. Figure 5 (b) shows XANES spectra taken *in situ* for a $(U_{0.93}Th_{0.07})O_2$ sample. Comparatively, there is a much smaller change observed between the spectra taken at 25$^o$C and 340$^o$C for the $(U_{0.93}Th_{0.07})O_2$ sample. Where $E_{WL,25^oC}$ = 17.159 keV and $E_{WL,340^oC}$ = 17.160 keV, corresponding to a $\Delta E_{WL}$ = 1 eV. This lower $\Delta E_{WL}$ observed likely corresponds to the formation of U(V). This shift correlates with the formation of extremely weak intensity intermediate oxide reflections, attributed to $U_4O_9$/$U_3O_7$ formation.

X-ray photoelectron spectroscopy (XPS) measurements were conducted for several samples following oxidation. Whilst the oxidative phase transition had been found to be reservable [13], this reduction requires heating in the presence of hydrogen. As this process was not carried out, it can be assumed that the samples are in the same state when measured by XPS as they were immediately following the *in situ* oxidation experiment. Fitted XPS spectra of the U-$4f_{7/2}$ photoemission lines for the $(U_{0.98}Th_{0.02})O_2$ and $(U_{0.87}Th_{0.13})O_2$ samples following heating, after 5 minutes sputtering the surface, are shown in Figure 6, with fitting parameters displayed in Table 1. The fit for the $(U_{0.98}Th_{0.02})O_2$ sample for the U-$4f_{7/2}$ core level suggests three valence states, U(IV)/(V)/(VI). This fit was conducted by fixing the areas of the U(V) and U(VI) components in a 2:1 ratio, as is expected for the orthorhombic phase of $U_3O_8$ [24]. The U(VI) and U(V) component positions have been fixed at approximately 383 eV and 382 eV, respectively [25]. However, there is a clear peak shoulder on the lower binding energy side of the emission line, which cannot be fitted with the U(V)/U(VI) components, suggesting there is U(IV) present in the sample. Therefore, a U(IV) component was added to the overall fit at approximately 380 eV [24]. A suitable fit was achieved by also allowing a slightly higher proportion of U(VI), producing a 2:1.2 U(V):U(VI) ratio with a small proportion of U(IV), making up approximately 15% of the total area. These results suggest that the small amount of thorium present in

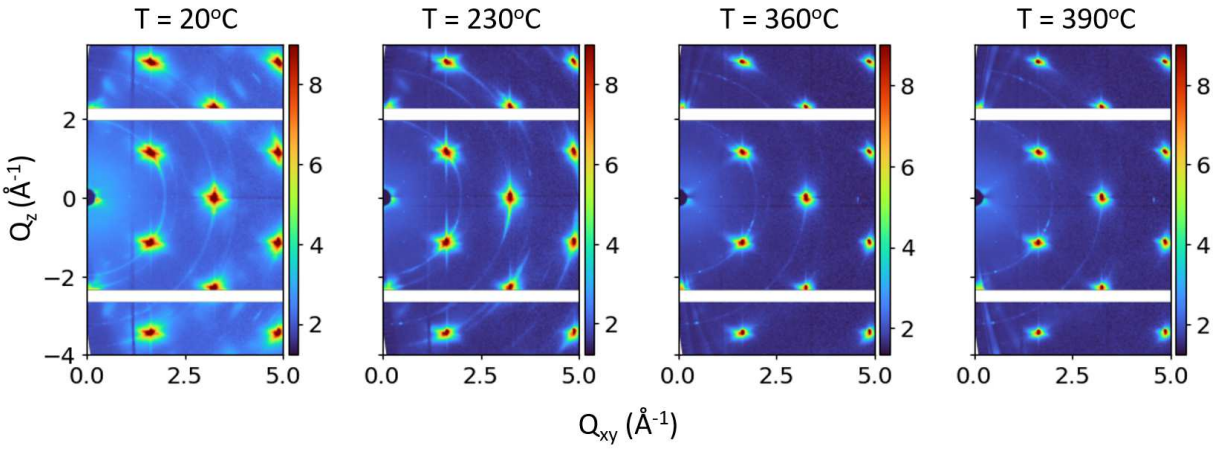



Figure 4: RSM showing *in situ* heating of $(U_{0.87}Th_{0.13})O_2$ [0 0 1]-oriented sample, showing the film at 20°C, 230°C, 360°C and 390°C. Slices were taken from he $Q_x = Q_y$ plane, showing the $(hhl)$ slice of the actinide oxide structure.

Table 1: X-ray photoemission U-$4f_{7/2}$ line fit values for the $(U_{0.98}Th_{0.02})O_2$ and $(U_{0.87}Th_{0.13})O_2$ samples following 5 minutes sputtering the surface.

| Sample | Peak | Proportion (%) | Position (eV) ($\pm$ 0.1 eV) | FWHM (eV) ($\pm$ 0.1 eV) | GL (%) |
|---|---|---|---|---|---|
| $(U_{0.98}Th_{0.02})O_2$ | IV | 15 | 380.0 | 1.8 | 30 |
| | V | 54 | 382.6 | 1.8 | 30 |
| | VI | 31 | 383.5 | 1.9 | 30 |
| $(U_{0.87}Th_{0.13})O_2$ | IV | 100 | 380.1 | 1.8 | 30 |

the lattice is preventing the oxidation of a small amount of uranium above a U(IV) valence state. This seems to be balanced by a slightly higher proportion of U(VI) than is usually found in $U_3O_8$. Fits of the U-$4f_{7/2}$ spectra for the $(U_{0.87}Th_{0.13})O_2$ sample shown in Figure 6, suggest that uranium is in a U(IV) oxidation state and that the bulk of the film is stoichiometric.

## 3. Discussion

*In situ* oxidation measurements of the $(U_{0.98}Th_{0.02})O_2$ sample indicated $U_3O_8$ formation, with several differences in both the structural transformation and the resultant uranium valency. According to the U-$4f_{7/2}$ spectra for the $(U_{0.98}Th_{0.02})O_2$ the presence of thorium effects the mixed-valency of the $U_3O_8$ phase which is formed, with the photoemission line presenting a tri-valency of U(IV)/(V)/(VI) as opposed to the expected U(V)/(VI). These results indicate that the 2% thorium present in the lattice is preventing an amount of uranium from oxidising, despite allowing the overall phase transition to $U_3O_8$. In addition, the remaining U(IV) is in a much higher proportion than the Th composition of 2%. The U(V):(VI) ratio in the $(U_{0.98}Th_{0.02})O_2$ sample is close to the expected ratio for orthorhombic $U_3O_8$, 2:1.2 as opposed to the expected 2:1 [5].

The differences in structural transformation observed for the $(U_{0.98}Th_{0.02})O_2$ sample are in relation to the formation of the intermediate phases $U_4O_9$ and $U_3O_7$. The satellite reflections appearing after heating to 230°C in Figure 1

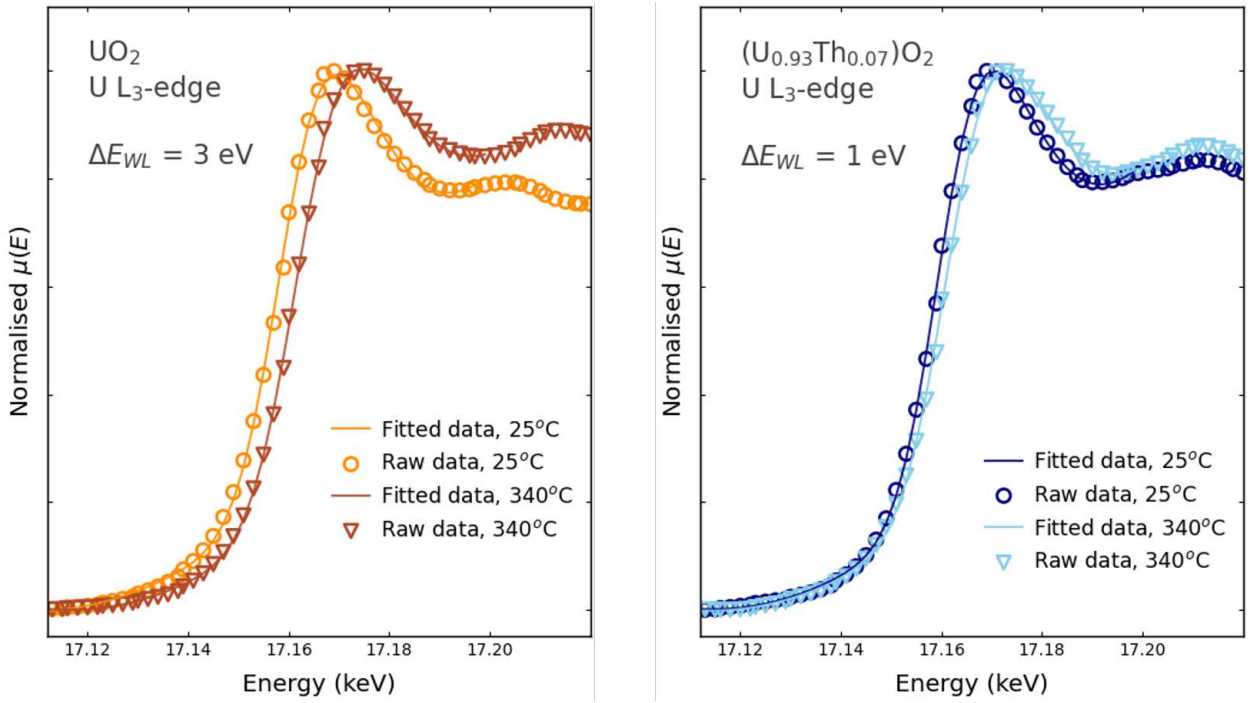



Figure 5: XANES spectra and fits taken at the U $L_3$-edge for a (a) $UO_2$ thin film sample at 25$^o$C and 340$^o$C shown in orange and red, respectively, and (b) $(U_{0.93}Th_{0.07})O_2$ sample at 25$^o$C and 340$^o$C shown in navy and blue, respectively.

are consistent with the expected reflections for the $\beta$-$U_4O_9$ structure [20]. As displayed in Figure 2, the $U_4O_9$ reflections present an unexpected weak broad peaks adjacent to the sharper superstructure where these broader peaks are not present in the the simulated map in Figure 2. As discussed by Lawrence Bright *et al.*, the sharper Bragg reflections are due to long-range ordering of uranium displacements by Willis clusters of oxygen interstitials, whereas the broader reflections are likely due to short-range ordering of the clusters themselves [19]. The unusual shape of these reflections for the mixed oxide is similar to that of $UO_2$, however there are additional expected $U_4O_9$ reflections missing in this work. This may suggest that long-range ordering of interstitial oxygen clusters is occurring in this case, as opposed to full formation of the weaker $U_4O_9$ superstructure, presumably due to the disruptive presence of Th(IV) in the lattice.

Reflections attributed to the $U_3O_7$ intermediate phase are only visible for the $(U_{0.98}Th_{0.02})O_2$ sample in the out-of-plane $Q_y = 0$ map at 313°C. In addition, the observed reflections are extremely weak, with several expected domains missing when compared to the calculated structure [4]. The experimental map also exhibits reflections which are not present in the $U_3O_7$ or $U_4O_9$ simulated maps. Comparatively, Lawrence Bright *et al.* [19] observed the formation of multiple crystallographic domains, visible both in-plane and out-of-plane, with results suggesting that $U_3O_7$ is epitaxially stable on the $UO_2$ (0 0 1) surface. However, despite the degree of $U_3O_7$ formation, Lawrence Bright still observes reflections present in the simulated maps which are not present in the experimental maps, and vice versa. Lawrence Bright suggests that the amount of epitaxial strain and inter-domain strain influences can impact the $U_3O_7$ structure observed. As discussed by Legg *et al.* in [12], the $CaF_2/(U_xTh_{1-x})O_{2+y}$ substrate/film system presents increasing epitaxial strain with respect to Th content. In addition, there are observed differences between the in-plane and out-of-plane strain, with a lattice contraction in-plane and a lattice expansion out-of-plane. Therefore, as $U_3O_7$ is tetragonal, different possible domains with different orientations will have different strains, meaning it could

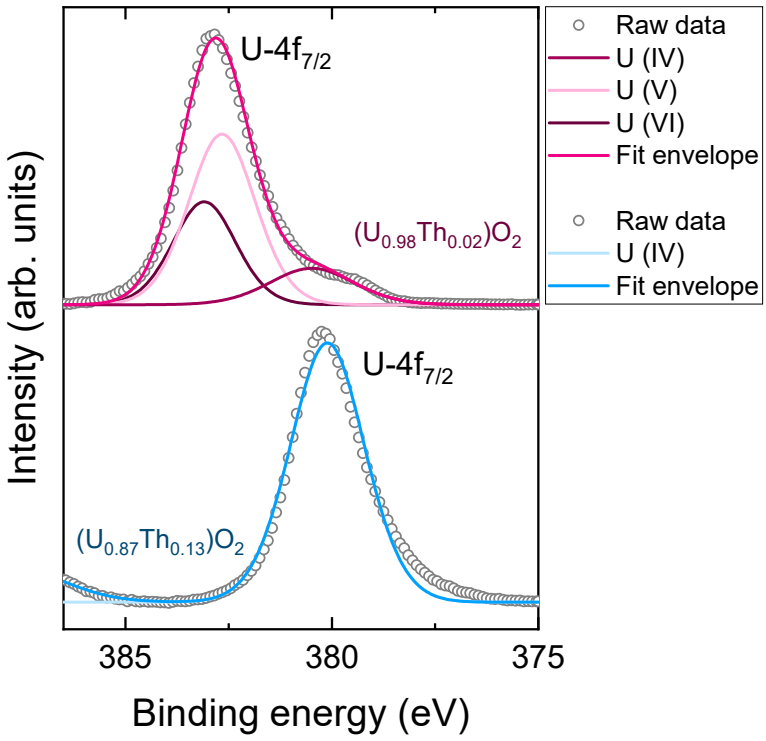



Figure 6: XPS spectra and fits for the U-$4f_{7/2}$ region for the oxidised $(U_{0.98}Th_{0.02})O_2$ and $(U_{0.87}Th_{0.13})O_2$ samples, shown in pink and blue, respectively. Spectra were collected following 5 minutes sputtering the film surface.

be possible that this increased asymmetry in strain due to thorium doping allows for greater formation of the $U_3O_7$ structure in one particular domain. However, it should also be noted that as $x$ = 0.98 the Th content is extremely low, meaning we should expect minimal added epitaxial strain compared to $UO_2$. Rickert *et al.* [11] observes some oxidation of bulk $(U_xTh_{1-x})O_2$ crystals where $x$ = 0.75 and 0.90, suggesting $U_4O_9$/$U_3O_7$ formation. In this study, it is unclear whether full formation of $U_3O_7$ is achieved. Therefore, we are unable to suggest whether the lack of full $U_3O_7$ formation is due to the thin film system or a result of the U-Th mixed oxide.

There are two possibilities which could explain the decreased $U_3O_7$ formation in the mixed oxide system, with respect to thin film properties. Firstly, the thin films investigated in this study are much thinner than those investigated by Lawrence Bright *et al.*, approximately 50 nm as opposed to 300 nm. As $U_3O_7$ superstructure reflections are weakly scattering, the reduced sample volume used in this study may have decreased the visibility of these reflections. However, significant $U_4O_9$ superstructure reflections were observed, which are also expected to scatter weakly. Additionally, the excellent epitaxial match between $CaF_2$ and $(U_xTh_{1-x})O_2$ may not allow incorporation of the significant distortion of the film lattice required to form the tetragonal $U_3O_7$ phase.

Chemical characterisation results for the $(U_{0.93}Th_{0.07})O_2$ sample suggest an intermediate stage of oxidation with respect to Th composition. For this sample, some formation of weaker intensity $U_3O_7$ reflections are observed in the out-of-plane maps. However, following this no higher oxide phases are formed. XANES results at the U $L_3$-edge for

the $(U_{0.93}Th_{0.07})O_2$ and $UO_2$ samples, shown in Figure 5, suggest some change to the U valency after heating. The $UO_2$ sample shown in Figure 5 (a) exhibits a $\Delta E_{WL}$ of 3 eV, suggesting U(VI) formation, correlated by the formation of $U_3O_8$ reflections at 340$^o$C. Comparatively, the $(U_{0.93}Th_{0.07})O_2$ sample exhibits a much smaller $\Delta E_{WL}$ of 1 eV, suggesting oxidation up to U(V). These results suggest that there is a significant barrier to U(VI) formation, which appears to occur at extremely low Th compositions. This combined with the structural measurements suggest that the degree of oxidation is tightly controlled by the thorium composition, where extremely low contents can significantly affect the U-valency, even where the structural transformation occurs.

The $(U_{0.87}Th_{0.13})O_2$ sample showed no evidence of oxidation in the film bulk. These results suggest that with a thorium dopant concentration of 13%, oxidation of $UO_2$-$UO_{2+y}$ to any higher oxide phase is entirely prevented. Both RSM and XPS results indicate that the $(U_{0.87}Th_{0.13})O_2$ sample remains as an FCC structure with predominately U(IV) valency following heating to 390°C. It also appears that the U valency which can be reached, i.e. whether formation of U(V) or U(VI) can be achieved, is tightly controlled by the Th composition, evidenced by the different degrees of U chemical transformation observed across the three $x$ = 0.87, 0.93 and 0.98 $(U_xTh_{1-x})O_2$ samples. This in turn suggests that the lack of structural transformation is due to a lack of interstitial O clusters leading to no long-range ordering of uranium displacements preventing the distortions required to form the $U_4O_9$ and $U_3O_7$ structures. As specifically the formation of $U_3O_7$ requires a high density of local interstitial O clusters to transform into the distorted $U_3O_7$ structure, it is possible that the remaining U(IV) shown in the spectra in Figure 6 means that the required interstitial O clusters cannot be formed and therefore allow full $U_3O_7$ formation. These results suggest that the lack of oxidation observed in the $(U_{0.87}Th_{0.13})O_2$ film is due to Th(IV) atoms in uranium lattice sites, leading to fewer $O^{2-}$ ions able to be accommodated in interstitial sites [26]. At this thorium composition, if we assume homogeneous distribution of Th in U lattice sites there will be approximately 1-2 Th atoms out of 14 per unit cell, where theoretically additional $O^{2-}$ could still be accommodated, suggesting that the inhibition of oxidation must be due to more factors than the lack of Th oxidation and of neighbouring U atoms. It is therefore also possible that the small amount of thorium in the unit cell disrupts the mobility of oxygen throughout the structure, preventing the formation of interstitial O clusters and in turn the ability to form long-range ordering.

The oxidative phase transition of U-Th mixed oxides has been investigated in several existing studies [6, 9, 10]. The majority of these studies observe a decrease in oxidation rate with respect to Th composition in a bulk mixed-oxide system. Alternatively, other studies observe an inhibition of oxidation to higher oxides such as $U_3O_8$, with some formation of $U_4O_9$ and $U_3O_7$, at higher Th compositions than seen in this work [11]. Rickert *et al.* suggests this lack of oxidation is due to an inability to charge balance further interstitial oxygen clusters due to Th atoms sitting in U lattice sites, similar to our findings. However, we observe a full inhibition of oxidation to both intermediate and higher oxide phases, arguably more significantly than has been seen in existing studies. This is likely due to the nature of the samples themselves, where we are utilising thin films comprised of high quality U-Th solid solutions with a very high degree of homogeneity. In addition to the sample morphology leading to significant inhibition, the nature of the samples has also allowed us to probe the effect of Th composition on subtler crystallographic relationships, such as the formation of the intermediate oxides. It is understood that the rate of oxidation in $UO_2$ powders is closely related to the grain boundary density [23, 27], with higher rates of oxidation observed in powders with finer grains. As we have no grains to consider in the epitaxial thin film sample system, our work also provides a more detailed understanding of the intra-granular oxidation process. Therefore, despite the degree of homogeneity and resultant inhibition likely not being achieved to the same extent for U-Th MOx on an industrial scale, the use of thin films in this case has allowed us to interrogate how Th effects the entire oxidative phase transition.

## 4. Conclusions

The oxidation of $UO_2$ can lead to complications with its safe and secure storage and a waste form, due to a significant volume expansion and an increase in solubility of the spent fuel matrix. In this work, we study whether the incorporation of thorium can inhibit the oxidation of $UO_2$. We utilise a series of epitaxial $(U_xTh_{1-x})O_2$ thin films, where $x$ = 0.87, 0.93 and 0.98 to measure the chemical and structural transformations associated with this phase transition using *in situ* XRD and XANES and *ex situ* XPS. These measurements were conducted on the ID11 and XMaS beamlines at the ESRF.

Oxidation from the FCC $(U_xTh_{1-x})O_2$ mixed-oxide is entirely inhibited where $x$ = 0.87, with no evidence of structural transformation in RSM or changes to U(IV) valency from XPS. Full transformation to $U_3O_8$ was observed where $x$ = 0.98, however several differences in the transition were observed, with significantly reduced formation of the intermediate $U_3O_7$ phase and U(IV) valency remaining in the final film. A significant decrease in oxidation is observed where $x$ = 0.93, with XANES results suggesting oxidation to U(IV)/(V) mixed valency but U(VI) formation is prevented. The overall results suggest that the inhibited oxidation observed in the mixed-oxide is due to fewer uranium in the lattice being unable to charge balance interstitial oxygen clusters, as well as a small amount of Th in the lattice sites effecting the mobility of oxygen throughout the structure, in turn preventing the structural distortions required to form the intermediate oxide structures.

These results have allowed us to closely interrogate the effect of Th on the entire oxidative phase transformation, allowing analysis of subtler aspects of the transition such as intermediate phase formation. In addition, these findings provide a more detailed insight into the the oxidative phase transition of $UO_2$ itself. Overall, the addition of thorium appears to significantly improves the long-term stability of $UO_2$ as a spent fuel, suggesting that a homogeneous solid solution of U-Th oxides would be suitable candidate for disposal-MOx.

## 5. Experimental Methods

### *5.1. Sample Fabrication*

Epitaxial [0 0 1]-oriented $(U_xTh_{1-x})O_2$ films, where $x$ = 0.87 and 0.98, investigated in this study have been previously characterised using XRD, x-ray reflectivity (XRR) and spectroscopic ellipsometry in [12], and using XPS in [26]. Additional thin film samples where $x$ = 0.93 and 1 were fabricated at the University of Bristol FaRMS for use in the XMaS beamline experiment presented in this study. These samples were heated under vacuum following growth to improve the initial oxide stoichiometry. All samples are [0 0 1]-oriented and form an epitaxial match with a $CaF_2$ substrate. Experimental work was carried out on the ID11 and XMaS beamlines at the ESRF. ID11 measurements provided high resolution structural characterisation, whereas measurements conducted on the XMaS beamline allowed correlation of structural and chemical transformations occurring throughout oxidation.

*5.2. In-situ oxidation*

Measurements on the ID11 nano-focus beamline were acquired using a fixed position Dectris Eiger CdTe 4M detector at a distance of 200 mm from the sample. A photon beam energy of 45.738 keV (0.27107 Å wavelength) was utilised with an in-plane diffraction geometry, as described in [19]. Thin film samples were heated in air using a PT100 resistive heater, calibrated to 400°C. Experimental data were taken as 2D mappings of still XRD images, collected with in-plane diffraction via azimuthal rotation about the axis perpendicular to the sample surface, with an angular step size of 0.1° and an acquisition time of 2 s/step.

Additional measurements were conducted on the XMaS beamline, probing both structural and chemical changes in the system. This was achieved by performing both XRD and XANES measurements at each temperature stage. XRD measurements were conducted at a photon energy of 16.2 keV, in grazing-incidence geometry at an incidence angle of 1°, via 270° azimuthal rotation about the axis perpendicular to the sample surface. XANES measurements were conducted in fluorescence mode at the U $L_3$-edge (17.17 keV).

The 2D XRD images collected were converted to RSM for analysis using custom software [19]. These were compiled by calculating the $q$ vector for each pixel in a frame, and selecting data points which fell within $\pm$ 0.02 $Å^{-1}$ of the map plane. The intensities for each of these points were corrected for polarisation and incident beam flux and plotted in an array. Simulated RSM were calculated for $U_4O_9$ and $U_3O_7$ to compare to experimental maps. Simulated maps for known structures were generated from published structures [4, 20] using the "Dans_Diffraction" Python package [28].

*5.3. X-ray photoelectron spectroscopy*

Mixed-oxide samples where $x$ = 0.87 and 0.98 were chemically characterised following heating using XPS. Measurements were conducted at the NanoESCA facility at the University of Bristol, using a ScientaOmicron Argus spectrometer with a monochromatic Al K$\alpha$ x-ray source [29]. Measurements were collected using a dwell time of 0.5 s, a step size of 0.05 eV and a pass energy of 100 eV using a 200 $\mu$m aperture. This combination leads to an overall energy resolution of approximately 700 meV at full-width-half-maximum. Measurements were conducted on the as-loaded film surface and following 5 minutes sputtering using a focused ion beam source (1 kV $Ar^+$ ions, 1 x 1 mm raster field, 2.6 $\mu$A beam current). A charge neutraliser was used for all measurements with a consistent beam energy of 3 eV, due to the insulating properties of $ThO_2$. The adventitious C-1s peak, fixed at 285.1 eV [30], was used to calibrate binding energy positions for the samples following measurements, and the intensity scale was corrected for the instrument transmission function [29].

## Author Contributions Statement

**F.L.:** Conceptualisation, sample fabrication, *in situ* oxidation experiments (ID11 & BM28) and data analysis, XPS data collection and analysis, figures, original draft preparation. **E.L.B.:** Conceptualisation, *in situ* oxidation experiments (ID11 & BM28) and data analysis, manuscript review and editing. **L.M.H.** Sample fabrication, *in situ* oxidation experiments (ID11 & BM28), XPS data analysis, manuscript review and editing. **D.W.:** *In situ* oxidation experiment (BM28). **J.L.:** XPS data collection and analysis. **E.H.:** *In situ* oxidation experiment (BM28). **H.G.:** Project supervision. **H.S.:** Project supervision, funding acquisition. **R.S.:** Conceptualisation, project supervision, funding acquisition.

## Acknowledgements

This work was conduced under the EPSRC, UK Centre for Doctoral Training in Nuclear Energy Futures grant EP/S023844/1, industrially co-sponsored by Sellafield Ltd. The experimental work was conducted at the ESRF at the ID11 and BM28 beamlines under the experimental proposals IH-MA-337 and A28-1-1468, respectively. XMaS/BM28 is a UK National Research Facility funded by EPSRC, via the grant EP/Y031962/1, operated by the Universities of Liverpool and Warwick. The authors would like to thank the beamline staff for support in conducting measurements. Sample synthesis was conducted at the University of Bristol FaRMS (EP/V035495/1), where access was awarded through the NNUF C1-2 user access scheme. XPS measurements were carried out at the University of Bristol NanoESCA Facility.

## Conflict of Interest Declaration

The authors declare that there is no known conflict of interest regarding the work presented in this article. No known financial or personal interests have had influence over the work presented here.

## Data Availability

ID11 [31] and BM28 [32] *in situ* oxidation data will be made publicly available following an embargo period.

## References

[1] T. K. Campbell, E. R. Gilbert, C. K. Thornhill, B. J. Wrona, Oxidation behavior of spent $UO_2$ fuel, Nuclear Technology 84 (2) (1989) 182–195. arXiv:https://doi.org/10.13182/NT89-A34186, doi:10.13182/NT89-A34186.
URL https://doi.org/10.13182/NT89-A34186

[2] J. Nakamura, T. Otomo, T. Kikuchi, S. Kawasaki, Oxidation of fuel rod under dry storage condition, Journal of Nuclear Science and Technology 32 (4) (1995) 321–332. arXiv:https://doi.org/10.1080/18811248.1995.9731712, doi:10.1080/18811248.1995.9731712.
URL https://doi.org/10.1080/18811248.1995.9731712

[3] R. Springell, E. L. Bright, D. A. Chaney, L. M. Harding, C. Bell, R. C. C. Ward, G. H. Lander, A review of uranium-based thin films, Advances in Physics 0 (0) (2023) 1–79. arXiv:https://doi.org/10.1080/00018732.2023.2230292, doi:10.1080/00018732.2023.2230292.
URL https://doi.org/10.1080/00018732.2023.2230292

[4] G. Leinders, R. Delville, J. Pakarinen, T. Cardinaels, K. Binnemans, M. Verwerft, Assessment of the $U_3O_7$ crystal structure by x-ray and electron diffraction, Inorganic Chemistry 55 (19) (2016) 9923–9936, pMID: 27648937. arXiv:https://doi.org/10.1021/acs.inorgchem.6b01941, doi:10.1021/acs.inorgchem.6b01941.
URL https://doi.org/10.1021/acs.inorgchem.6b01941

[5] G. Leinders, R. Bes, J. Pakarinen, K. Kvashnina, M. Verwerft, Evolution of the uranium chemical state in mixed-valence oxides, Inorganic Chemistry 56 (12) (2017) 6784–6787, pMID: 28590135. arXiv:https://doi.org/10.1021/acs.inorgchem.7b01001, doi:10.1021/acs.inorgchem.7b01001.
URL https://doi.org/10.1021/acs.inorgchem.7b01001

[6] E. S. A. Galperin, M. Todosow, Assessment of homogeneous thorium/uranium fuel for pressurized water reactors, Nuclear Technology 138 (2) (2002) 111–122. arXiv:https://doi.org/10.13182/NT01-21, doi:10.13182/NT01-21.
URL https://doi.org/10.13182/NT01-21

[7] M. Cole, L. Blackburn, L. Haigh, D. Bailey, L. Townsend, K. Kvashnina, N. Hyatt, C. Corkhill, A disposal-MOX concept for plutonium disposition, Mater. Adv. 5 (2024) 6416–6425. doi:10.1039/D4MA00420E.
URL http://dx.doi.org/10.1039/D4MA00420E

[8] J. Herring, P. MacDonald, K. Weaver, C. Kullberg, Low cost, proliferation resistant, uranium-thorium dioxide fuels for light water reactors, Nuclear Engineering and Design 203 (1) (2001) 65–85. doi:https://doi.org/10.1016/S0029-5493(00)00297-1.
URL https://www.sciencedirect.com/science/article/pii/S0029549300002971

[9] P. A. Demkowicz, J. L. Jerden, J. C. Cunnane, N. Shibuya, R. Baney, J. Tulenko, Aqueous dissolution of urania-thoria nuclear fuel, Nuclear Technology 147 (1) (2004) 157–170. arXiv:https://doi.org/10.13182/NT04-A3522, doi:10.13182/NT04-A3522.
URL https://doi.org/10.13182/NT04-A3522

[10] S. Sunder, N. Miller, XPS and XRD studies of (Th,U)$O_2$ fuel corrosion in water, Journal of Nuclear Materials 279 (1) (2000) 118–126. doi:https://doi.org/10.1016/S0022-3115(99)00242-1.
URL https://www.sciencedirect.com/science/article/pii/S0022311599002421

[11] K. Rickert, T. Prusnick, E. Hunt, M. Kimani, S. Chastang, D. Brooks, E. Moore, J. Petrosky, J. Mann, Inhibiting laser oxidation of $UO_2$ via Th substitution, Journal of Nuclear Materials 517 (2019) 254–262. doi:https://doi.org/10.1016/j.jnucmat.2019.02.005.
URL https://www.sciencedirect.com/science/article/pii/S0022311518316702

[12] F. Legg, L. Harding, J. Lewis, R. Nicholls, H. Green, H. Steele, R. Springell, Epitaxial light actinide oxide thin films, Thin Solid Films 790 (2024) 140194. doi:https://doi.org/10.1016/j.tsf.2023.140194.
URL https://www.sciencedirect.com/science/article/pii/S0040609023005278

[13] J. Wasik, R. Podor, J. Lewis, N. Cuffe, C. Beer, C. Bell, R. Springell, A topotactic phase transition in the uranium oxide system, arXiv preprint arXiv:2607.07291 (2026).

[14] W. Thomas, F. Wilhelm, S. Langridge, L. M. Harding, C. Bell, R. Springell, S. Friedemann, R. Caciuffo, G. H. Lander, Absence of induced ferromagnetism in epitaxial uranium dioxide thin films, Phys. Rev. B 109 (2024) 064420. doi:10.1103/PhysRevB.109.064420.
URL https://link.aps.org/doi/10.1103/PhysRevB.109.064420

[15] L. Harding, E. Lawrence Bright, J. Laverock, D. Goddard, R. Springell, Epitaxial stabilisation of uranium silicide line compounds, Thin Solid Films 768 (2023) 139690. doi:https://doi.org/10.1016/j.tsf.2023.139690.
URL https://www.sciencedirect.com/science/article/pii/S0040609023000214

[16] E. Lawrence Bright, S. Rennie, M. Cattelan, N. Fox, D. Goddard, R. Springell, Epitaxial UN and $\alpha$-$U_2N_3$ thin films, Thin Solid Films 661 (2018) 71–77. doi:https://doi.org/10.1016/j.tsf.2018.07.018.
URL https://www.sciencedirect.com/science/article/pii/S0040609018304814

[17] D. N. Batchelder, R. O. Simmons, Lattice Constants and Thermal Expansivities of Silicon and of Calcium Fluoride between 6° and 322°K, The Journal of Chemical Physics 41 (8) (2004) 2324–2329. arXiv:https://pubs.aip.org/aip/jcp/article-pdf/41/8/2324/11177745/2324_1_online.pdf, doi:10.1063/1.1726266.
URL https://doi.org/10.1063/1.1726266

[18] M. M. Strehle, B. J. Heuser, M. S. Elbakhshwan, X. Han, D. J. Gennardo, H. K. Pappas, H. Ju, Characterization of single crystal uranium-oxide thin films grown via reactive-gas magnetron sputtering on yttria-stabilized zirconia and sapphire, Thin Solid Films 520 (17) (2012) 5616–5626. doi:https://doi.org/10.1016/j.tsf.2012.04.022.
URL https://www.sciencedirect.com/science/article/pii/S0040609012004531

[19] E. Lawrence Bright, L. Harding, R. Springell, G. Lander, Crystallographic transformation of $UO_2$ to $U_4O_9$, $U_3O_7$, and $U_3O_8$, Acta Materialia 319 (2026) 122642. doi:https://doi.org/10.1016/j.actamat.2026.122642.
URL https://www.sciencedirect.com/science/article/pii/S1359645426007421

[20] R. I. Cooper, B. T. M. Willis, Refinement of the structure of $\beta$-$U_4O_9$, Acta Crystallographica Section A 60 (4) (2004) 322–325. doi:10.1107/S010876730401219X.
URL https://doi.org/10.1107/S010876730401219X

[21] B. T. M. Willis, Crystallographic studies of anion-excess uranium oxides, J. Chem. Soc., Faraday Trans. 2 83 (1987) 1073–1081. doi:10.1039/F29878301073.
URL http://dx.doi.org/10.1039/F29878301073

[22] P. Q. Duan, H. L. Bao, J. Li, H. J. Cao, Y. Y. Huang, In-situ high-energy-resolution x-ray absorption spectroscopy for uo2 oxidation at ssrf, Nuclear Science and Techniques 28 (1) (2017) 2. doi:10.1007/s41365-016-0155-x.
URL https://link.springer.com/article/10.1007/s41365-016-0155-x

[23] E. De Bona, K. Popa, O. Walter, M. Cologna, C. Hennig, A. C. Scheinost, D. Prieur, Oxidation of micro- and nanograined uo2 pellets by in situ synchrotron x-ray diffraction, Inorganic Chemistry 61 (4) (2022) 1843. doi:10.1021/acs.inorgchem.1c02652.
URL https://pmc.ncbi.nlm.nih.gov/articles/PMC9052414/

[24] E. S. Ilton, P. S. Bagus, XPS determination of uranium oxidation states, Surface and Interface Analysis 43 (13) (2011) 1549–1560. arXiv:https://analyticalsciencejournals.onlinelibrary.wiley.com/doi/pdf/10.1002/sia.3836, doi:https://doi.org/10.1002/sia.3836.
URL https://analyticalsciencejournals.onlinelibrary.wiley.com/doi/abs/10.1002/sia.3836

[25] E. L. Bright, L. Xu, L. M. Harding, R. Springell, A. C. Walters, M. Sundermann, M. Garcia-Fernandez, S. Agrestini, R. Caciuffo, G. van der Laan, G. H. Lander, Resonant inelastic x-ray scattering from $U_3O_8$ and UN, Journal of Physics: Condensed Matter 35 (17) (2023) 175501. doi:10.1088/1361-648X/acb8f4.
URL https://dx.doi.org/10.1088/1361-648X/acb8f4

[26] F. Legg, L. M. Harding, E. Lawrence Bright, D. Wermeille, P. Smith, J. Laverock, H. Green, H. Steele, R. Springell, Improving the long term durability of $UO_2$ wasteforms through thoria doping, Journal of Nuclear Materials 632 (2026) 156875. doi:https://doi.org/10.1016/j.jnucmat.2026.156875.
URL https://www.sciencedirect.com/science/article/pii/S002231152600440X

[27] M. Liu, Q. Kang, H. Xu, Grain-scale study of the grain boundary effect on $UO_2$ fuel oxidation and fission gas release under reactor conditions, Chemical Engineering Science 229 (2021) 116026. doi:https://doi.org/10.1016/j.ces.2020.116026.
URL https://www.sciencedirect.com/science/article/pii/S0009250920305583

[28] "dans diffraction". doi:https://doi.org/10.5281/zenodo.3752479.

[29] J. Laverock, N. A. Fox, Quantitative model of internal analyzer scattering in a hemispherical electron analyzer and its application to improve the accuracy of the transmission function, Surface and Interface Analysis 58 (7) (2026) 456–470. doi:https://doi.org/10.1002/sia.70069.
URL https://analyticalsciencejournals.onlinelibrary.wiley.com/doi/10.1002/sia.70069

[30] S. Van den Berghe, F. Miserque, T. Gouder, B. Gaudreau, M. Verwerft, X-ray photoelectron spectroscopy on uranium oxides: a comparison between bulk and thin layers, Journal of Nuclear Materials 294 (1) (2001) 168–174, 10th Int. Symp. on Thermodynamics of Nuclear Materials. doi:https://doi.org/10.1016/S0022-3115(01)00461-5.
URL https://www.sciencedirect.com/science/article/pii/S0022311501004615

[31] Mixed thorium / uranium oxide thin films [dataset], european Synchrotron Radiation Facility (2026). doi:10.15151/ESRF-ES-1084898347.
URL https://doi.org/10.15151/ESRF-ES-1084898347

[32] Investigating the structural and chemical properties in the oxidation of u-th mox [dataset], european Synchrotron Radiation Facility (2028). doi:10.15151/ESRF-ES-2249471705.
URL https://doi.org/10.15151/ESRF-ES-2249471705

**Figure and Table Captions**

Figure 1: RSM showing the oxidation of [0 0 1]-oriented $(U_{0.98}Th_{0.02})O_2$ sample at 20°C, 230°C, 360°C and 390°C. Slices have been taken from the $Q_x = Q_y$ plane, showing the $(hhl)$ slice of the actinide oxide structure.

Figure 2: (a) Simulated RSM of $U_4O_9$ structure [20] compared to experimental map for the $(U_{0.98}Th_{0.02})O_2$ sample at 298°C. (b) A close up of one $U_4O_9$ reflection is shown in the experimental map (as indicated by the red square), compared to the equivalent simulated reflection

Figure 3: (a) Simulated RSM of the $U_3O_7$ structures [4] compared to an experimental map for the $(U_{0.98}Th_{0.02})O_2$ sample at 313°C. (b) A close up of two reflections as indicated in the experimental map by the red square, compared to the equivalent area for simulated $U_3O_7$ and $U_4O_9$ maps.

Figure 4: RSM showing *in situ* heating of $(U_{0.87}Th_{0.13})O_2$ [0 0 1]-oriented sample, showing the film at 20°C, 230°C, 360°C and 390°C. Slices were taken from the $Q_x = Q_y$ plane, showing the $(hhl)$ slice of actinide oxide structure.

Table 1: X-ray photoemission U-$4f_{7/2}$ line fit values for the $(U_{0.98}Th_{0.02}O_2$ and $(U_{0.87}Th_{0.13})O_2$ samples following 5 minuted sputtering the surface.

Figure 5: XANES spectra and fits taken at the U $L_3$-edge for a (a) $UO_2$ thin film sample at 25°C and 340°C shown in navy and blue, respectively.

Figure 6: XPS spectra and fits for the U-$4f_{7/2}$ region for the oxidised $(U_{0.98}Th_{0.02}$ and $(U_{0.87}Th_{0.13})O_2$ samples, shown in pink and blue, respectively. Spectra were collected following 5 minuted sputtering the film surface.